

Direct ambient photopatterning of RGB quantum dots for light-emitting diodes with EQE exceeding 20%

Received: 26 April 2025

Accepted: 24 September 2025

Published online: 03 November 2025

 Check for updates

Jie Guan^{1,7}, Jianhang Ma^{1,7}, Likuan Zhou², Yihao Zou¹, Lingbin Ye³, Wenjun Hou⁴, Pan-ke Zhang^①, Xingliang Dai^③, Hao Zhang^⑤, Dmitri V. Talapin^⑥✉ & Yuanyuan Wang^①✉

Optical patterning of quantum dots is essential for the fabrication of light-emitting diodes displays. However, current patterning methods either require inert environments or compromised quantum dots optical properties under ambient conditions. Here, we report a photoresist-free strategy enabling direct quantum dot patterning in air by using triphenylphosphine, a cost-effective, commercially available molecule that functions simultaneously as a surface ligand, photoinitiator, and oxidation protector. Under light exposure, triphenylphosphine reacts with atmospheric oxygen to trigger solubility changes, allowing precise patterning with resolutions up to 9534 dpi. The resulting devices exhibit external quantum efficiencies of 21.6% (blue), 25.6% (green), and 20.2% (red). We further demonstrate full-color active-matrix quantum dots light-emitting diodes displays by integrating the patterned red, green and blue quantum dots with thin-film transistor backplanes. This work offers a scalable, non-destructive, and environmentally compatible patterning solution for industrial display technologies.

Colloidal quantum dots (QDs), with their tunable emission wavelengths, high color purity, and excellent optoelectronic properties, are redefining the core architecture of next-generation display technologies^{1–3}. In recent years, the commercialization of quantum dots light-emitting diodes (QLEDs) has accelerated advances in both emissive materials and device structures, particularly in terms of brightness, resolution, and energy efficiency^{4–6}. The next-generation of QLED technologies increasingly relies on electroluminescence (EL) from red, green, and blue (RGB) QD arrays, which places stringent requirements on the spatial precision of QD patterning^{7–9}. This requirement becomes especially critical for microdisplay applications

such as augmented reality and virtual reality, where pixel sizes fall below 10 μm . These applications demand ultrahigh-density QD pattern alignment, presenting dual challenges: achieving sub-micrometer patterning resolution while maintaining compatibility with environmentally benign, scalable processing conditions^{10,11}.

While techniques such as transfer printing^{12,13} and inkjet printing^{14,15} are widely used in large-area device fabrication, they fall short of delivering the sub-micrometer resolution required for advanced micro-displays. In contrast, direct optical lithography for functional inorganic nanomaterials (DOLFIN) offers a promising route to achieving high-resolution QDs patterning^{16–20}. This technique relies

¹State Key Laboratory of Coordination Chemistry, School of Chemistry and Chemical Engineering, Nanjing University, Nanjing, China. ²National Center of Technology Innovation for Display, Guangdong Juhua Research Institute of Advanced Display, Guangzhou, China. ³Wenzhou Key Laboratory of Novel Optoelectronic and Nano Materials and Engineering Research Centre of Zhejiang Province, Institute of Wenzhou, Zhejiang University, Wenzhou, P. R. China. ⁴TCL Research, Shenzhen, China. ⁵Department of Chemistry, Center for BioAnalytical Chemistry, Key Laboratory of Bioorganic Phosphorus Chemistry & Chemical Biology of Ministry of Education, Tsinghua University, Beijing, China. ⁶Department of Chemistry, Pritzker School of Molecular Engineering, and James Franck Institute, University of Chicago, Chicago, IL, USA. ⁷These authors contributed equally: Jie Guan, Jianhang Ma.

✉ e-mail: dvtalapin@uchicago.edu; wangyy@nju.edu.cn

on light-triggered changes in QDs solubility mediated by surface chemistry to define patterns in selected regions. However, under ambient conditions, ultraviolet (UV) exposure inevitably leads to surface oxidation or photodegradation of QDs, which severely compromises their optical properties^{21,22}. As a result, most current patterning approaches still require inert gas environments, limiting the practical applicability of such technologies. Moreover, the photosensitive ligands commonly in use require complex synthetic processes and are unable to simultaneously provide surface passivation and light responsiveness^{23,24}. These limitations are particularly problematic for blue-emitting QDs, whose patterned devices consistently underperform. For instance, the external quantum efficiency (EQE) of patterned blue QLEDs typically drops below 12%, markedly lower than the >20% EQE achievable with unpatterned films (Supplementary Table 1). Recent efforts have focused on designing air-stable photoactive molecule crosslinking agents^{25–27}. However, these molecules function merely as an additive, involves complex synthesis, lacks compatibility with blue-emitting QDs, and leads to suboptimal device performance.

To address the aforementioned challenges in commercializing QDs patterning, there is a need to develop multifunctional molecules that are structurally simple for fabrication, require less stringent synthesis conditions, can operate in ambient environments, and maintain high optical properties and device performance at the same time. Such molecules must simultaneously fulfill multiple roles: efficiently passivate surface trap states, enable spatially selective photoactivation under UV light, and provide robust oxidative protection. Additionally, they must be compatible with existing QDs ink formulations and function reliably under ambient (non-inert) conditions. Ideally, these ligands should be readily available and cost-effective as well.

Among various ligand systems, phosphorus-containing molecules have long played a central role in QDs chemistry, particularly in synthesis and surface engineering^{28–31}. Representative examples such as trioctylphosphine (TOP) and triphenylphosphine (TPP) are commonly employed as coordinating solvents and reductants during QDs growth, as well as surface-passivating agents that enhance photoluminescence efficiency and colloidal stability^{32,33}. TPP has attracted attention for its moderate electron-donating ability, chemically stable aromatic structure, and compact molecular size, all of which contribute to its excellent compatibility with various QDs compositions^{34,35}. Despite these advantages, the potential of TPP in post-synthetic QDs processing has remained largely unexplored.

Here, we present a molecular-level multifunctional patterning strategy for the direct optical lithography of QDs under ambient conditions. This strategy integrates surface passivation, oxidative protection, and photoactivation into a single small-molecule design (Fig. 1). This design overcomes the limitations of conventional photosensitive ligands that deactivate in air and enables high-resolution, non-destructive patterning without the need for inert atmospheres. Upon UV exposure, TPP undergoes oxygen-mediated photoactivation, triggering a synergistic light-induced reaction that enables spatially precise modulation of QDs solubility. This mechanism allows patterning with a resolution reaching 9534 dots per inch (dpi), while preserving the structural and optical integrity of the QDs. Leveraging this strategy, we fabricate high-performance RGB-patterned QLEDs (non-arrayed), achieving EQE of 21.6% for blue QLEDs along with 25.6% for green and 20.2% for red. Furthermore, we demonstrate the full-color active-matrix QLEDs display based entirely on directly optical patterned QDs by integrating the RGB arrays with a thin-film transistor (TFT) backplane. Importantly, this work marks the successful demonstration of direct patterning of blue QDs and their integration into TFT circuits. The method also exhibits excellent compatibility with TFT backplanes across various pixel dimensions, including $85 \times 140 \mu\text{m}$ and $380 \times 650 \mu\text{m}$, underscoring its strong potential for multifunctional device fabrication. This work bridges laboratory-scale molecular design with practical device engineering, offering a scalable,

cost-effective, and environmentally compatible solution for next-generation electroluminescent QLEDs display fabrication.

Results

Multi-functionality of triphenylphosphine molecules

TPP is highly soluble in non-polar solvents and can be added directly to the desired QDs solution to prepare photosensitive inks. The resulting core-shell QDs-TPP in nonpolar solvents exhibits good dispersion and stability (Fig. 2a). The absorption and photoluminescence (PL) spectra of red-, green-, and blue-emitting QDs (Fig. 2b) show size-dependent exciton features that does not change after addition of TPP to the pristine QDs (Supplementary Fig. 1). The fluorescence properties of the QDs after TPP treatment are significantly improved (Fig. 2c). The photoluminescence quantum yields (PLQYs) of the RGB-emitting QDs-TPP are 96.1%, 94.9%, and 90.0%, respectively. For comparison, the PLQYs of pristine QDs are 80.2%, 81.0%, and 75.6% (Supplementary Table 2). The time-resolved carrier dynamics and averaged PL lifetimes trend strongly correlate with the PLQYs results (Fig. 2d–f). After TPP treatment, the average PL lifetime of RGB-emitting QDs increase from 26.8, 20.0, and 14.8 ns to 28.4, 23.0, and 18.3 ns, respectively, indicating that surface defects are effectively passivated, thus reducing the proportion of non-radiative recombination (Supplementary Table 3). These results clearly demonstrate that the addition of TPP helps improve surface passivation and enhances optical performance¹⁵. We further observe that when the mass fraction of TPP exceed 5%, the PLQYs of QDs reach a plateau rather than continuing to increase or decrease. This suggests that the presence of excess TPP in the ink does not compromise the optical properties of the QDs (Supplementary Fig. 2).

We further compare the morphology and size of pristine red-, green-, and blue-emitting QDs and QDs-TPP (Fig. 2g and Supplementary Figs. 3 and 4). The morphology and size of QDs-TPP remain unchanged, implying that the preparation process of photosensitive ink has no destructive effect on QDs. The exciton features of core-shell QDs are indistinct in absorption spectra, making changes difficult to observe. To ensure reliable conclusions, we study wurtzite CdSe QDs, monitoring their absorption spectra before and after TPP passivation. The clearly resolved excitonic features and unchanged emission spectrum prove that no etching or shell growth occurred during TPP treatment (Supplementary Fig. 5), which is also determined from transmission electron microscopy (TEM) images (Supplementary Fig. 6).

The interaction between QDs and TPP is further verified by Fourier-transformed infrared (FTIR) spectra. Figure 2h shows the FTIR spectra corresponding to pristine CdSe/ZnS QDs, TPP, and CdSe/ZnS QDs-TPP. Upon incubation in TPP solution, the QDs show three distinct FTIR bands at 3060 cm^{-1} , 1476 cm^{-1} , and 1010 cm^{-1} (blue curve), which could arise from the stretching vibrations of phosphorus atom and C-H bond on the benzene ring, C=C on the benzene ring and C-P stretching vibration in TPP (green curve), respectively³⁶. Further evidence of the interaction between QDs and TPP is elaborated by using bare CdSe/ZnS QDs to eliminate the interference of original organic ligands (e.g., oleic acid (OA) or oleylamine, etc.). As expected, the vibrational peaks of the OA surface ligands completely disappear in bare CdSe/ZnS QDs (Supplementary Fig. 7). Compared with that of bare CdSe/ZnS QDs (black curve), the characteristic peaks belonging to TPP (red curve) appear in the FTIR spectra of QDs-TPP (blue curve).

We then explore the anchoring sites of TPP on the QDs surface through nuclear magnetic resonance (NMR) spectroscopy. Generally, phosphine-based molecules serve as L-type ligands attached to metal (M) sites on the QD surface³⁷. However, the steric size of the ligand strongly influences its ligand binding affinity. In particular, due to its large cone angle and low ligand basicity, TPP has a weaker binding affinity to QDs than OA/oleylamine³⁸. Therefore, we infer that TPP would be more inclined to passivate non-metal (E) sites rather than

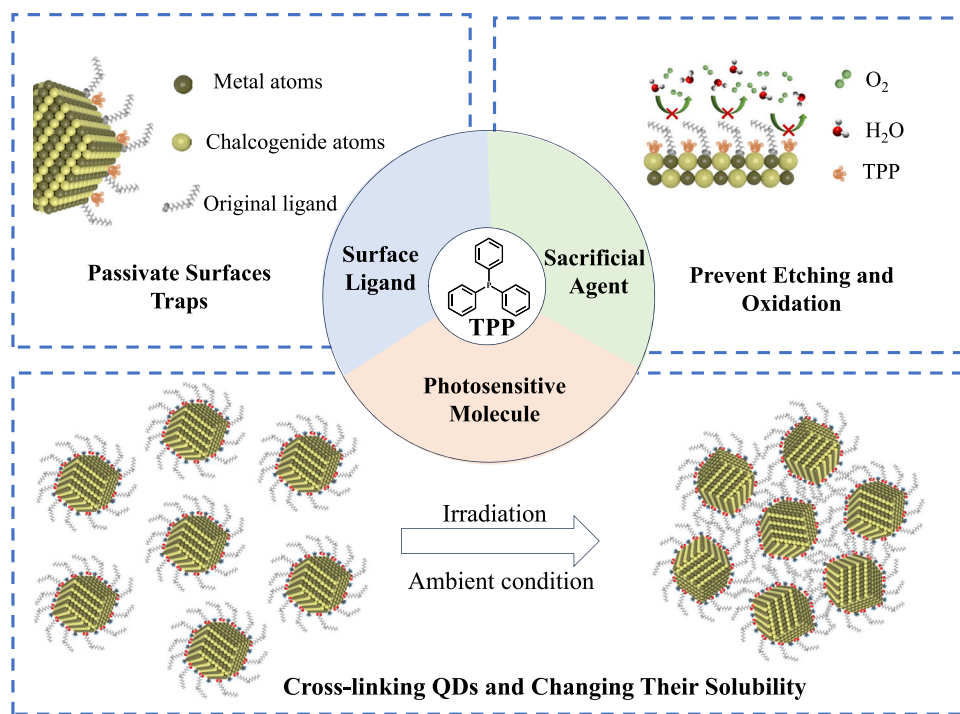


Fig. 1 | Schematic illustration of the role of multifunctional molecules. TPP molecules can serve simultaneously as surface ligands, sacrificial agents, and photoinitiators.

replace the original ligands on the surface of QDs. To test this hypothesis, we compare the ^{31}P NMR spectra of bare CdSe QDs before and after their interaction with TPP (Fig. 2i). We find that when bare CdSe QDs interact with TPP, a new peak at -35.5 ppm appears in the ^{31}P NMR spectra in addition to the characteristic peak of free TPP at -6.7 ppm (blue curve). By comparison with the ^{31}P signal of TPP-Se (red curve), it is determined that the change is due to the interaction of TPP with the E site of CdSe QDs, which is consistent with our previous report³⁹. Since the optical properties of colloidal QDs directly determined the properties of QDs films, improving the PLQYs of pristine QDs in solution should be one of the effective ways to enhance the performance of patterned QDs.

Radical reactions play a key role in the cross-linking of organic ligands on the surface of QDs. Several research teams have achieved QDs cross-linking through reactive radical intermediates^{24,40,41}. Inspired by the fact that TPP can be used as a photoinitiator for the photopolymerization of acrylic resin³³, we hypothesize that in addition to serving as surface ligands to improve the optical properties of QDs, TPP also has the potential to initiate ligand cross-linking reactions under UV light as photosensitive molecules. Our experiments further confirm this hypothesis: the solubility of QDs changes after UV exposure in the presence of TPP (Supplementary Fig. 8).

To investigate this process in detail, we systematically analyze the effect of UV irradiation QDs-TPP system. The UV-visible absorption spectrum reveals that TPP exhibits strong absorption at 254 nm, while its absorption in the UV-A region (320–400 nm) is relatively weak (Supplementary Fig. 9). Electron paramagnetic resonance (EPR) analysis demonstrates that TPP generates free radicals under UV irradiation at 254 nm and 365 nm (Fig. 3a and Supplementary Fig. 10). Since the radicals are highly unstable, N-tert-Butyl-alpha-phenylnitron (PBN) is used as spin traps. The EPR spectrum shows no signal for TPP in the absence of light (black solid curve), but a strong radical signal appears after UV irradiation at 254 nm (red solid curve). By comparing with simulated spectra, we identify the signal sources as diphenylphosphine (blue dashed curve) and phenyl radicals (green dashed curve). Moreover, after irradiating a toluene solution containing TPP

and OA, the radical signal significantly decreases (Supplementary Fig. 11), suggesting that OA may interact with free radicals.

We propose two possible mechanisms for this interaction. The first hypothesis is that radicals induce polymerization of the C=C double bond in OA. However, further experiments rule out this possibility: as shown in Fig. 3b, the ^1H NMR spectrum of the TPP-OA mixture in toluene- d_8 indicates that the characteristic peak at -5.5 ppm remains unchanged after UV irradiation at 254 nm, suggesting that sterically hindered C=C double bond in OA does not participate in the reaction. Additionally, we synthesize CdSe QDs capped solely with stearic acid (which lacks C=C double bonds) and successfully achieve QDs patterning using TPP under ambient conditions (Supplementary Fig. 12), further disproving the hypothesis of radical-induced polymerization of OA double bonds.

An alternative mechanism involves radical reactivity with saturated hydrocarbon groups. The QDs patterning process requires the presence of O_2 (Supplementary Fig. 13). Pattern cannot be achieved within the glove box, indicating that TPP and O_2 may synergistically mediate the radical reaction. Based on these findings, we propose a mechanism for TPP-mediated ligand cross-linking. Under UV irradiation, TPP act as a photoinitiator, inducing the formation of carbon-centered radicals from alkyl ligands on the QDs surface⁴². These carbon radicals rapidly react with O_2 , generating peroxy radicals ($\text{OO}\cdot$), which subsequently trigger ligand cross-linking reactions⁴³. Then, hydroxyl radicals ($\cdot\text{OH}$) form sequentially promote chain propagation by reacting with alkanes to complete the ligand cross-linking process⁴⁴. To monitor the presence of $\cdot\text{OH}$ radicals, we employ terephthalic acid (TA) as a probe, which forms the fluorescent product 2-hydroxyterephthalic acid upon reaction with $\cdot\text{OH}$ ⁴⁵. As shown in Fig. 3c, the PL intensity of probe TA at 430 nm increases remarkably with prolonged irradiation time under 325 nm UV excitation, (Fig. 3c), confirming the continuous production of $\cdot\text{OH}$ and gradual accumulation of the fluorescent TA derivative. Further supporting evidence is proved by X-ray photoelectron spectroscopy (XPS) characterization. As shown in Supplementary Fig. 14, we compare the C1s peaks XPS spectra of QDs-TPP films before and after illumination, C-O-C bond

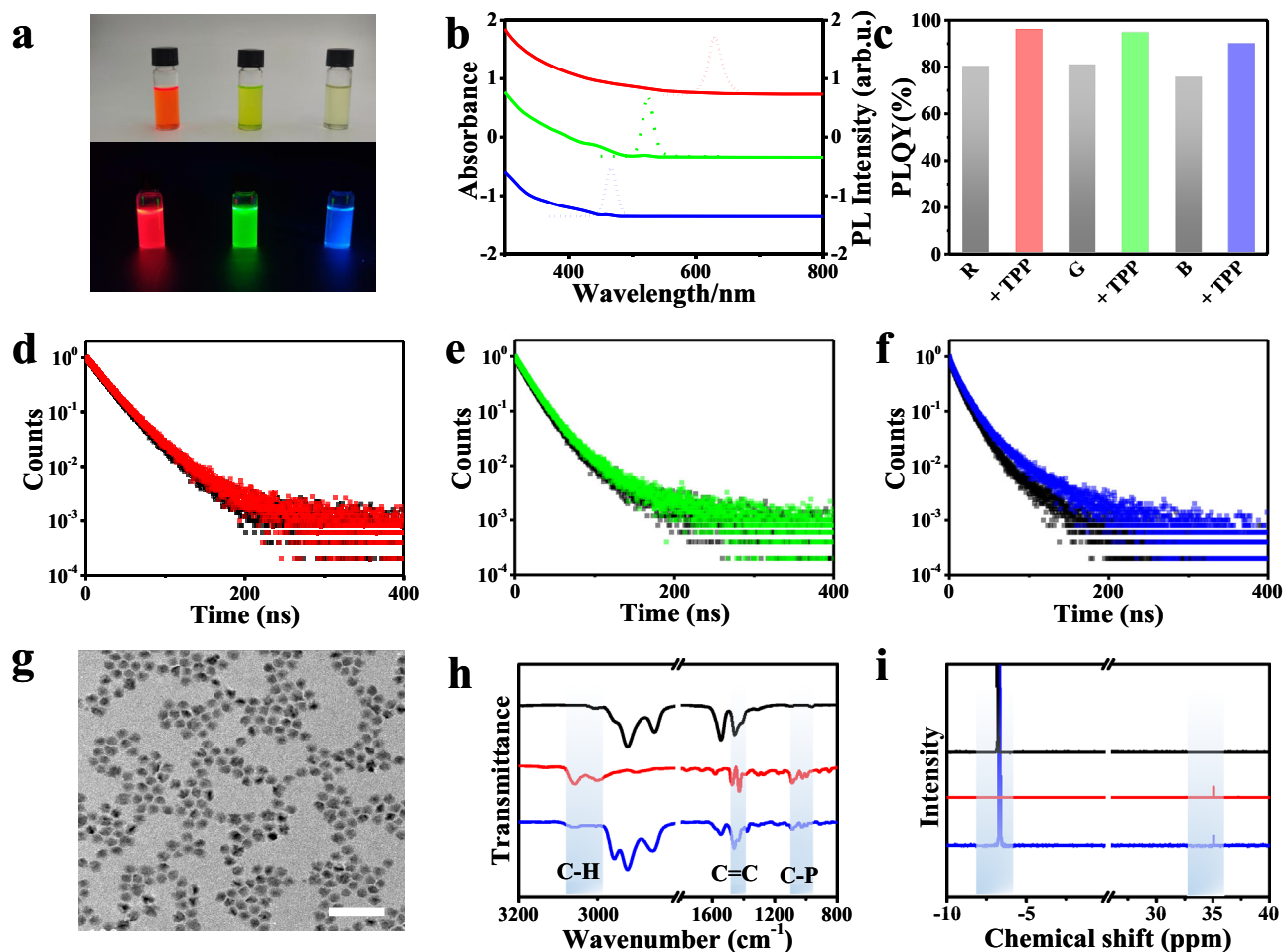


Fig. 2 | Surface ligands to passivate QDs via surface protection. **a** Photos of red, green, and blue-emitting QDs-TTP under visible light and UV light. **b** Absorption (solid lines) and PL (dashed lines) spectra of red, green, and blue-emitting QDs-TTP. **c** Comparison of PLQYs of red (**d**), green (**e**), and blue (**f**)-emitting QDs and QDs-TTP. Time-resolved PL decay profiles of red, green, and blue-emitting QDs solution

before and after treatment with TPP. **g** A TEM image of CdSe/ZnS QDs-TTP. Scale bar, 100 nm. **h** FTIR spectra of pristine CdSe/ZnS QDs (red curve), TPP (green curve), and CdSe/ZnS QDs-TTP (blue curve). **i** ^{31}P NMR spectra of free TPP (black curve), TPP-Se (red curve), bare CdSe QDs-TTP (blue curve).

appeared in the fitting⁴⁶. Therefore, it can be seen that under UV irradiation, TPP generates radicals that induce the formation of carbon-centered radicals from alkyl ligands on the surface of QDs. These radicals further react with O_2 to form peroxy radicals, which initiate ligand crosslinking reactions, ultimately enabling the patterning of QDs (Fig. 3d).

Previous studies indicate only modest photostability of QDs in air, primarily due to surface oxidation by O_2 from the atmosphere or solvents under illumination, leading to surface defects^{47,48}. For example, under UV exposure, the first excitonic transition peak of CdSe QDs shifts from 548 nm to 523 nm⁴⁹. Consequently, previous patterning processes have to be conducted inside gloveboxes or in low-oxygen, low-humidity environment to preserve the optical properties of QDs, which significantly increases the cost and complicated process scaleup^{20,23,25,50}.

The TPP molecule, as a reductant, can react with O_2 to form the corresponding oxide⁵¹. We find that light exposure accelerates this process. As shown in Fig. 4a, under 254 nm UV light, the absorption spectrum of TPP changes significantly, with the characteristic absorption peak at 263 nm decreasing and characteristic absorption peak at 266 nm appearing, indicating that the TPP molecule undergoes oxidation⁵². This process is further confirmed by ^{31}P NMR measurement. As illustrated in Fig. 4b, after light exposure, the phosphorus signal of the TPP molecule at -6.6 ppm significantly decreases,

indicating a reduction in the trivalent phosphorus content⁵³. Simultaneously, a new strong signal appears around 26 ppm, corresponding to pentavalent phosphorus, suggesting that part of the TPP is oxidized to form triphenylphosphine oxide (TPPO)⁵⁴. Therefore, we infer that TPP in the photosensitive ink preferentially reacts with oxygen in the air under UV light, acting as a sacrificial agent to protect QDs, thereby reducing chemical damage during the photo-oxidation process and enhancing the photostability of QDs.

To confirm the above hypothesis, we first use CdSe QDs as a model to compare their optical properties before and after light exposure. As shown in Fig. 4c, after exposure to 254 nm UV light in air, the pristine CdSe QDs exhibit an 8 nm blue shift in their characteristic absorption peak. This blue shift is mainly attributed to the desorption of surface ligands and/or photochemical oxidation of QDs surfaces under UV excitation, reducing the effective core size of the QDs⁵⁵. However, after the addition of TPP, the absorption peak of the QDs remains unchanged under the same conditions, which indicates that TPP efficiently inhibits the photo-oxidation of QDs surface. We further investigate the impact of TPP molecules on the photostability of core-shell QDs in an ambient environment. Although the growth of the shell layer can effectively enhance the stability of QDs, almost all types of QDs remain susceptible to oxygen and water under light excitation²². We find that addition of TPP can significantly improve the photostability of core-shell QDs. Figure 4d and Supplementary Fig. 15

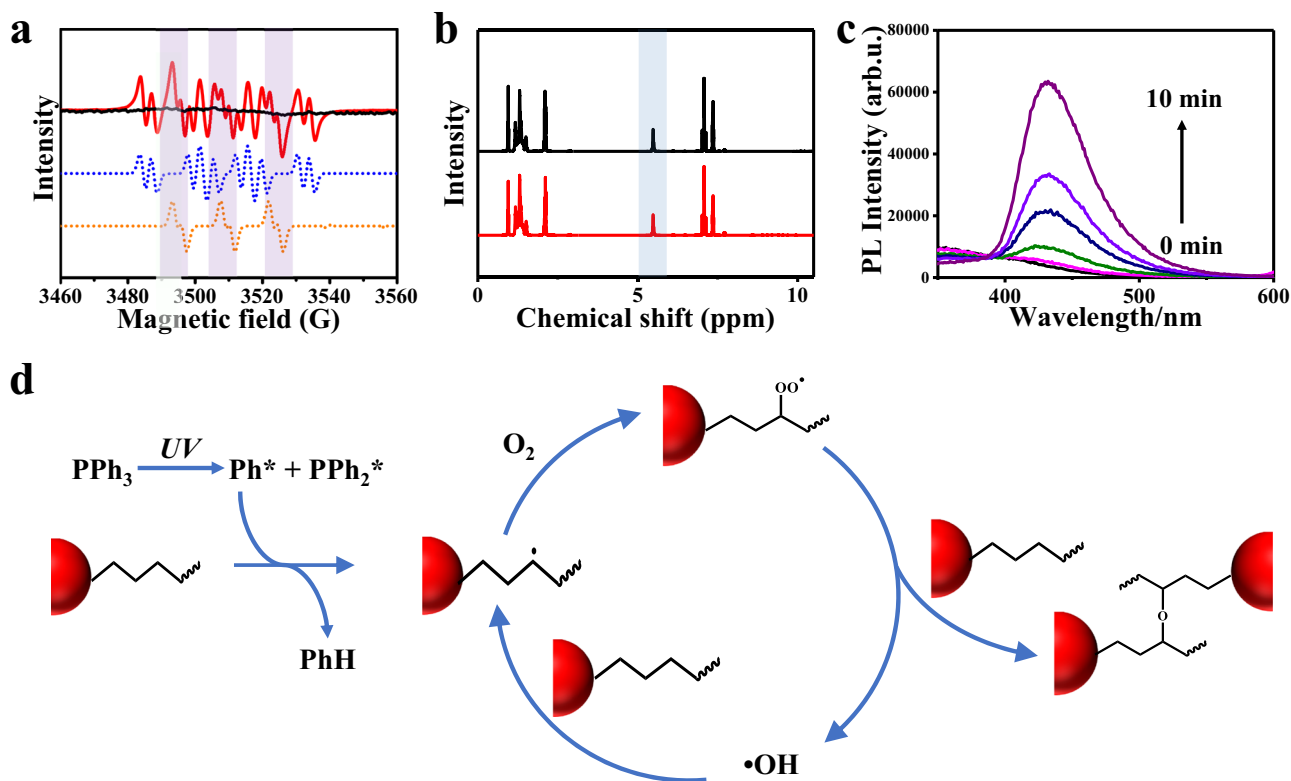


Fig. 3 | Photosensitive molecules to initiate ligand cross-linking reactions. **a** EPR spectra of TPP without (black curve) and with (red curve) 254 nm UV irradiation. The dashed lines represent the simulated spectra of diphenylphosphine (blue dashed curve) and phenyl radicals (green dashed curve). **b** ^1H NMR spectra of OA mixed with TPP without (black curve) and with (red curve) 254 nm UV

irradiation. **c** Changes in the PL spectrum of probe terephthalic acid solution as the concentration of $\cdot\text{OH}$ is increased upon excitation at 315 nm (from down to top: 0, 0.5, 1, 3, 5, and 10 min, respectively). **d** Potential mechanism of the photo cross-linking between ligands of QDs.

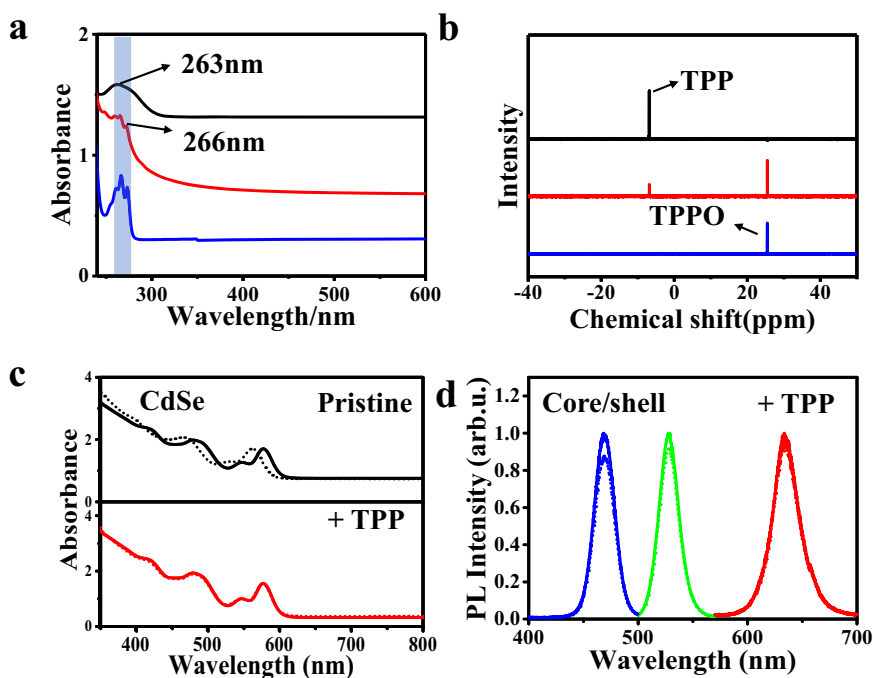


Fig. 4 | Sacrificial agents to protect QD films from damage during irradiation. **a** Absorption spectra of TPP (black curve), TPP after irradiated by 254 nm UV light (red curve), and TPPO (blue curve). **b** ^{31}P NMR spectra of free TPP (black curve), TPP after irradiated by UV (red curve), and TPPO (blue curve). **c** Absorption spectra of

pristine (black) CdSe QDs and QDs-TPP (red) before (solid) and after (dashed) UV irradiation. **d** PL spectra of red-, green-, and blue-emitting QDs-TPP before (solid) and after (dashed) UV irradiation.

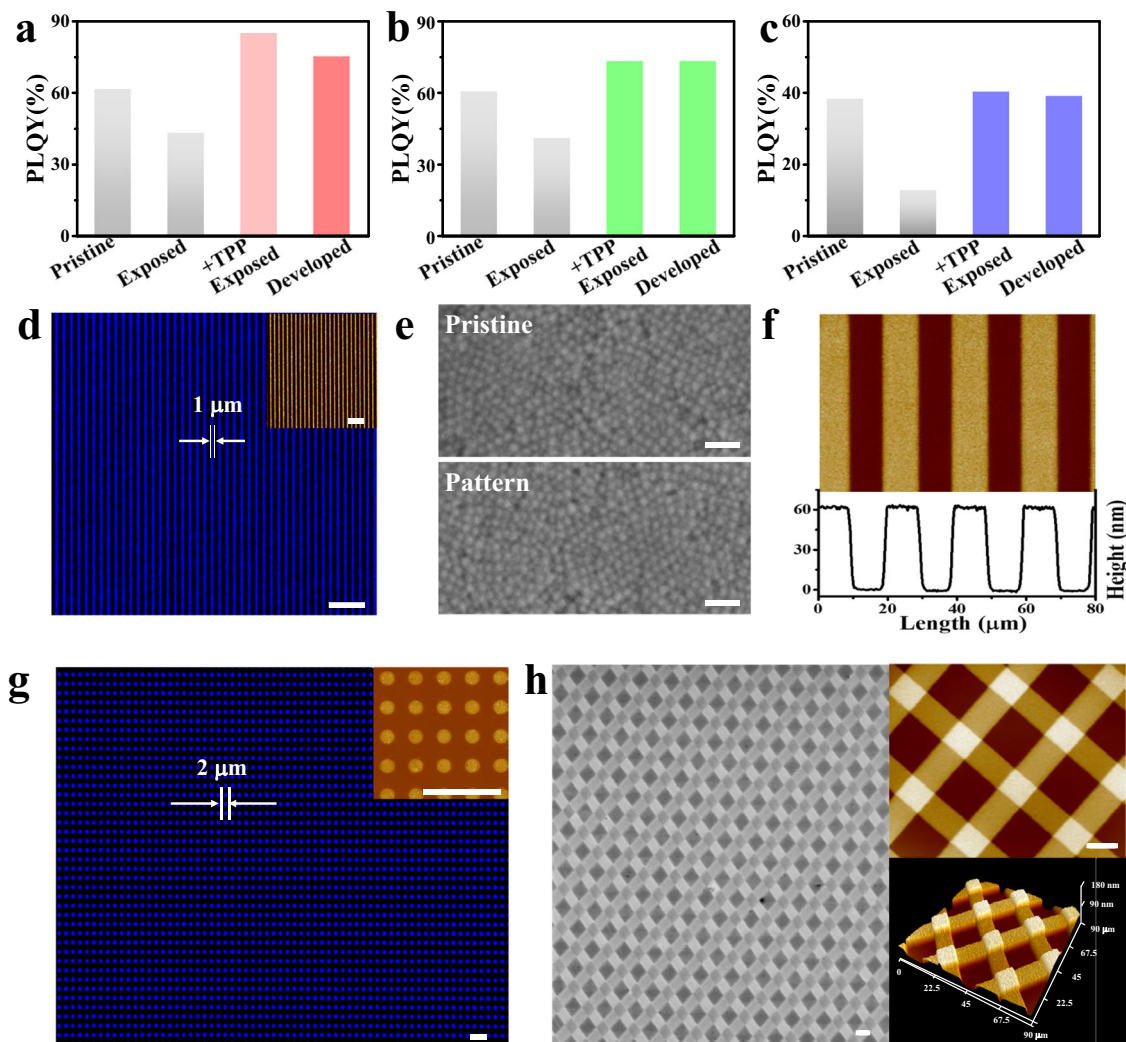


Fig. 5 | Non-destructive full-color patterning of QDs. Changes in PLQYs of red- (a), green- (b), and blue- (c) emitting QDs-TPP films at various stages for patterning. **d** patterned lines of blue-emitting QDs and an AFM image of lines patterns (inset). Scale bars, 10 μm. **e** SEM images of pristine and patterned QDs films. Scale bars,

50 μm. **f** Height profiles and an AFM image of line patterns. **g** Pixelated blue-emitting QDs and an AFM image of dots patterns (inset). Scale bars, 10 μm. **h** Images of SEM (left), AFM (right) of multilayer line patterns created by using red- and green-emitting QDs. Scale bars, 10 μm.

compare the fluorescence spectra of pristine red-, green-, and blue-emitting QDs and QDs-TPP films before and after exposure to 254 nm UV doses exceeding 200 mJ cm^{-2} . After adding TPP, the PLQYs of red-, green-, and blue-emitting QDs remain almost unchanged before and after UV exposure. In addition, even after exposure to a UV dose exceeding 2000 mJ cm^{-2} (254 nm), the emission peak position and full width at half maximum of QDs-TPP remain unchanged (Supplementary Fig. 16), demonstrating the protective effect of TPP on QDs.

Non-destructive full-color patterning of quantum dots

The absorption spectra, steady-state, and time-resolved PL spectra confirm that the photophysical properties of QDs-TPP remain unchanged when deposited into films. As shown in Supplementary Fig. 17, there are no significant shifts in the absorption and PL peaks. In addition, the PLQYs and lifetime are preserved or even improved for the red-, green-, and blue-emitting QDs films as shown in Supplementary Figs. 18 and 19. These are consistent with the results of the QDs solution.

Non-destructive approaches for QDs patterning are essential for achieving high-performance, pixelated optoelectronic devices. The multifunctional TPP molecules serve as surface ligands, photosensitizers, and sacrificial agents at the same time, allowing the QDs to

be directly implemented into the photoresist-free patterning process to achieve non-destructive multiscale full-color patterning. The effect of direct optical patterning on the optical properties of QDs is studied by monitoring the PLQYs of Cd-based QDs at various patterning steps (Fig. 5a–c). These stages comprise film deposition, UV exposure (exposed), and post-patterning development (developed). For comparison, PLQY values at each stage are normalized to the relative/remnant of initial PLQY and expressed as a percentage. As shown in Supplementary Fig. 20, QDs-TPP films largely preserve their PLQYs throughout the patterning steps, with red-, green-, and blue-emitting QDs-TPP retaining more than 85% under ambient conditions. By contrast, the corresponding QDs without TPP experience notable decreases in relative PLQY following 254 nm UV irradiation in air, maintaining only approximately 70% (red), 67% (green), and 60% (blue) of their initial values (Supplementary Fig. 21). Furthermore, we also have conducted specific evaluations of our patterning strategy on Cd-free QDs (Supplementary Fig. 22). The results are consistent with the phenomena observed in Cd-based QDs, which further demonstrates the superiority of TPP and highlighted the non-destructive nature of our approach.

Cross-linking significantly reduces the solubility of the QDs in the exposed regions in nonpolar solvents, providing the foundation for

patterning. Taking advantage of the fact that cross-linking can be initiated by free radicals generated by TPP under light, the QDs film is no longer dispersed in the developer after exposure, thus enabling the patterning of QDs. The design concept and parameter control of the patterning method allows efficient, high-resolution, and high-fidelity patterning of QDs. In our work, typical 254 nm UV doses for TPP patterning are 40–270 mJ cm⁻², superior to those for traditional photoresists¹⁶. The specific selection of TPP concentration and UV exposure dose is detailed in Supplementary Fig. 23. We observe a clear trend: increasing the TPP concentration leads to a reduction in the required UV dose for initiating effective crosslinking. This trend can be attributed to the higher density of photosensitizer molecules at elevated TPP concentrations, which facilitates more efficient radical generation under UV irradiation. As a result, less photonic energy is needed to trigger the crosslinking reaction. Conversely, at lower TPP concentrations, a higher UV dose is required to compensate for the reduced radical generation efficiency.

Stripe patterns with equal linewidth and dots patterns with equal spacing are fabricated to characterize the spatial resolution. Supplementary Fig. 24 shows high-resolution and uniform line patterns of different color QDs. The finest features are 1 μm, as shown in the line patterns, which completely replicate those of the photomasks (Fig. 5d). The above results demonstrate the patterning capabilities for QDs by photoresist-free patterning technology with TPP. Atomic force microscopy (AFM) images (Supplementary Fig. 25) are used to assess the quality of unpatterned and patterned QD films, revealing no significant changes in average surface roughness after patterning. Moreover, the patterning process does not affect the QD sizes or introduce observable pinholes or cracks (Fig. 5e). Scanning electron microscopic (SEM) images (Supplementary Fig. 26) display clear contrast between exposed and unexposed regions, confirming the complete removal of residual QDs after development. Figure 5f shows well-defined height profiles of line patterns with high uniformity, low surface roughness, and sharp edges (Fig. 5f). The line edge roughness of the line patterns is 156 nm (Supplementary Fig. 27), consistent with the result by SEM (Supplementary Fig. 28). The thickness of the patterned image is uniform and can reach ~60 nm as measured by the profilometer, and the root mean square roughness (Rq) is calculated to be 1.5 nm from the AFM data, showing a flat surface of the patterns.

The resolution of patterned pixel array can reach 9534 dpi (Fig. 5g and Supplementary Fig. 29). We should note that the resolution is determined by the smallest features in the photomask, rather than the properties of photosensitive inks. This implies that if the photomask features are sufficiently small, sub-micron patterning resolution could be achieved. In addition, the direct optical patterning of QDs-TPP inks allow complex pattern architectures to be constructed layer-by-layer sequentially through three steps per layer: ink coating, exposure, and development. The thicknesses of the individual patterned lines are approximately 95 nm and 115 nm, respectively. In the regions where the two 10 μm-wide lines overlap, the total thickness reaches 175 nm, confirming the successful layer-by-layer stacking (Supplementary Fig. 30). As shown in the SEM and AFM images in Fig. 5h, such layer-by-layer patterning enables the design of three dimensional (3D) inorganic layers with high vertical dimensional fidelity and excellent lateral resolution, demonstrating that our method has the ability to construct 3D structures of inorganic materials.

The present patterning approach renders well-defined QDs patterns of varying shapes and dimensions with high fidelity. Images of QDs films in the formats of complex logos, letters, and numbers patterned with 365 nm UV light demonstrate the versatility of our photolithography patterning method (Supplementary Fig. 31). The optical patterning process is described in Fig. 6a, which involves coating, exposure, and developing of QDs films. Figure 6b–d show clear, uniform fluorescence images of a parrot based on individual red-, green- and blue-emitting QDs. The vertical stacks of QDs patterns allows

combinations of RGB primary colors to generate multiple colors. Specifically, yellow is produced by sequentially patterning red- and green-emitting QDs, magenta by red- and blue-emitting QDs, and cyan by green- and blue-emitting QDs (Fig. 6e–g). The magnified view of fluorescent microscopic images in Fig. 6e–g show no color contamination, illustrating that the photoresist-free patterning method would not damage the underlying layer. In addition, patterns can also be achieved through a layer-by-layer process except for the sequential stacked process, which enables the richness of colors required for full-color imaging design (Supplementary Fig. 32). The patterning of the subsequent layer does not affect the morphological or optical properties of the underlying layers. The direct optical patterning method enables orthogonal processing by creating full-color images after the delicate pixel design through consecutive patterning processes (Fig. 6h). In addition to Cd-based QDs, the non-destructive photoresist-free patterning strategy also works well for other nanocrystals, such as heavy-metal-free QDs, metals, and oxides, respectively (Fig. 6i and Supplementary Fig. 33).

In the recent years, more attention is paid to flexible electronic devices, which provide additional possibilities for information, energy, medical, and other fields⁵⁶. Fig. 6j shows a QDs pattern on a highly flexible substrate (polyethylene terephthalate plastic film, PET plastic film), thus demonstrating suitability of our QDs inks for flexible (opto) electronic technologies. In addition, as shown in Fig. 6k, l, mild condition makes photoresist-free patterning seamlessly transferrable between flexible substrates (PET plastic film) and rigid substrates (ITO glass, silicon oxide wafer, etc.).

Furthermore, the design strategy for patterning QDs under ambient conditions with TPP can be extended. Given that TPP could generate effective radicals under UV irradiation and enable subsequent crosslinking, we validated this using several phosphine molecules with similar structures, such as TOP, dimethylphenylphosphine (DPP), and methyl(diphenyl)phosphine (MDP). Among them, trialkylphosphines (such as TOP) are not suitable for direct patterning. This is mainly because they lack significant absorption in the near-UV region (e.g., 254 nm), and thus cannot efficiently enhance the formation of radicals required for the oxygen-mediated crosslinking process. In contrast, DPP and MDP, due to their conjugated benzene rings, exhibit strong UV absorption (Supplementary Fig. 34). This allows them to act as effective photosensitizers to realize QDs pattern as well (Supplementary Fig. 35). Then, we compare the exposure dose required for patterning with the same mass fraction (30%) of phosphine molecules (Supplementary Fig. 36). We observe that their radical generation efficiency and patterning performance vary depending on molecular structure and substitution pattern. Therefore, while TPP remains the most effective candidate among those tested, our findings indicate that other aromatic phosphine compounds could also serve as viable alternatives, provided their structures are carefully tuned to achieve a delicate balance between UV absorption capacity, radical generation efficiency, and surface coordination affinity.

High performance of quantum dots light-emitting diodes

QDs exhibited narrow emission spectra and high PLQYs are suitable for high-performance QLEDs. Devices are fabricated using a hybrid charge transport architecture (Fig. 7a), in which poly(3,4-ethylenedioxy-thiophene) polystyrene sulfonate (PEDOT: PSS) and poly(9,9-dioctylfluorene-alt-N-(4-sec-butylphenyl)-diphenylamine) (TFB) serve as the hole injection layer and hole transport layer (HTL), respectively. The emissive layer consists of a 25 nm-thick crosslinked QD film prepared from a QDs dispersion containing 10 wt% TPP. A transparent ZnMgO nanoparticle layer functions as the electron transport layer (ETL). Further fabrication details are provided in the Supporting Information.

The steps of direct optical patterning of QDs with photoresist-free patterning technology adapt well to the established workflows for fabricating EL devices, allowing us to apply the patterned QDs as an

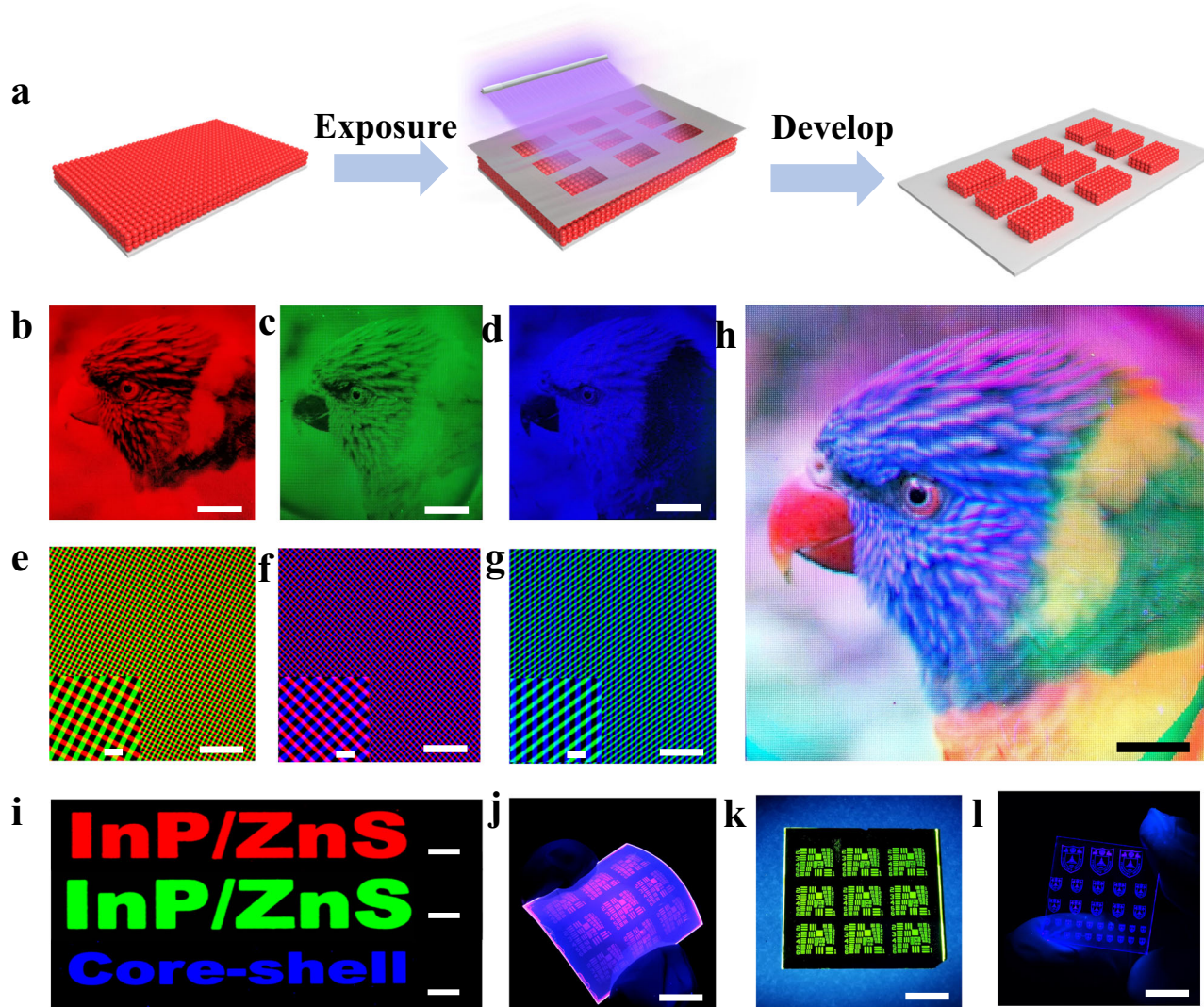


Fig. 6 | Patterns of QDs-TPP with 254 nm UV light. **a** Procedures for photoresist-free patterning. **b–d** Fluorescent microscopic images of red-, green-, and blue-emitting QDs parrot patterns. Scale bars, 5 mm. **e–g** Fluorescent microscopic images of yellow, magenta, and cyan line patterns. Inset: a magnified view of fluorescent microscopic images. Scale bars, 100 μm . **h** Fluorescence microscopic

image of colorful parrot pattern via consecutive steps. Scale bars, 5 mm. **i** Patterns made by different types of QDs. From top to bottom: red InP/ZnS, green InP/ZnS, blue ZnSe/ZnS. Scale bars, 100 μm . **j–l** Patterns on different substrates. From left to right: PET plastic film, silicon oxide wafer, and ITO glass. Scale bars, 5 mm.

emissive layer of the QLEDs device (non-arrayed) to test their EL performance. Figure 7b shows that crosslinked devices have the same EL emission peak (peak emission wavelength and the spectral linewidth) as pristine devices, indicating that the TPP-based patterning method is indeed non-destructive and effectively preserved the photophysical properties of the QDs. Furthermore, the patterned RGB QLEDs composed of 4 μm line arrays (insets of Fig. 7) further demonstrate the excellent adaptability of this method for high-definition display manufacturing. We further characterize the current density-voltage (J - V) behavior, luminance, and EQEs of pristine and crosslinked QLEDs. Both devices exhibit comparable performance, indicating that photocrosslinking with the employed TPP does not affect the optical or transport characteristics of QD films (Fig. 7c–h). In addition, crosslinked QLEDs demonstrate good EL performance, particularly for blue-emitting QLEDs. Representative current density-voltage-luminance (J - V - L) curves for pristine and crosslinked blue QLEDs are shown in Fig. 7e and h, maximum luminance values of 7851 and 7472 cd m^{-2} , and EQEs of 22.4% and 21.6%. Device lifetimes are also measured at different initial luminance (Supplementary Fig. 37), revealing that crosslinked blue-emitting QLEDs exhibit a T_{95} lifetime at 1000 nits of 135 h,

comparable to 159 h for pristine devices (Supplementary Fig. 38). While the crosslinked devices, especially blue-emitting ones, perform well, their characteristics remain below those of current state-of-the-art individual devices³⁷. Compared to other patterning methods, our work exhibits higher efficiency in crosslinked blue-emitting QLEDs, as shown in Supplementary Table 1. Our direct photolithography patterning method also extends to the fabrication of red- (Fig. 7c, f) and green-emitting (Fig. 7d, g) patterned QLEDs (non-arrayed). Similar comparisons apply to pristine and crosslinked red and green QLEDs. We demonstrate consistent results of the high EQEs for red- (20.2%) and green-emitting (25.6%) crosslinked QLEDs. A detailed comparison of QLEDs characteristics can be found in Supplementary Table 4, with all our RGB QLEDs among the best-performing crosslinked QLEDs, demonstrating that TPP-based photoresist-free patterning is a general approach for the fabrication of high-performance QLEDs displays and related integrated devices.

Previous works suggest that the photochemical process involved in direct photopatterning leads to a significant decrease of device performance after patterning⁵⁰. In our work, we employ multifunctional TPP, which minimize the performance loss caused by the

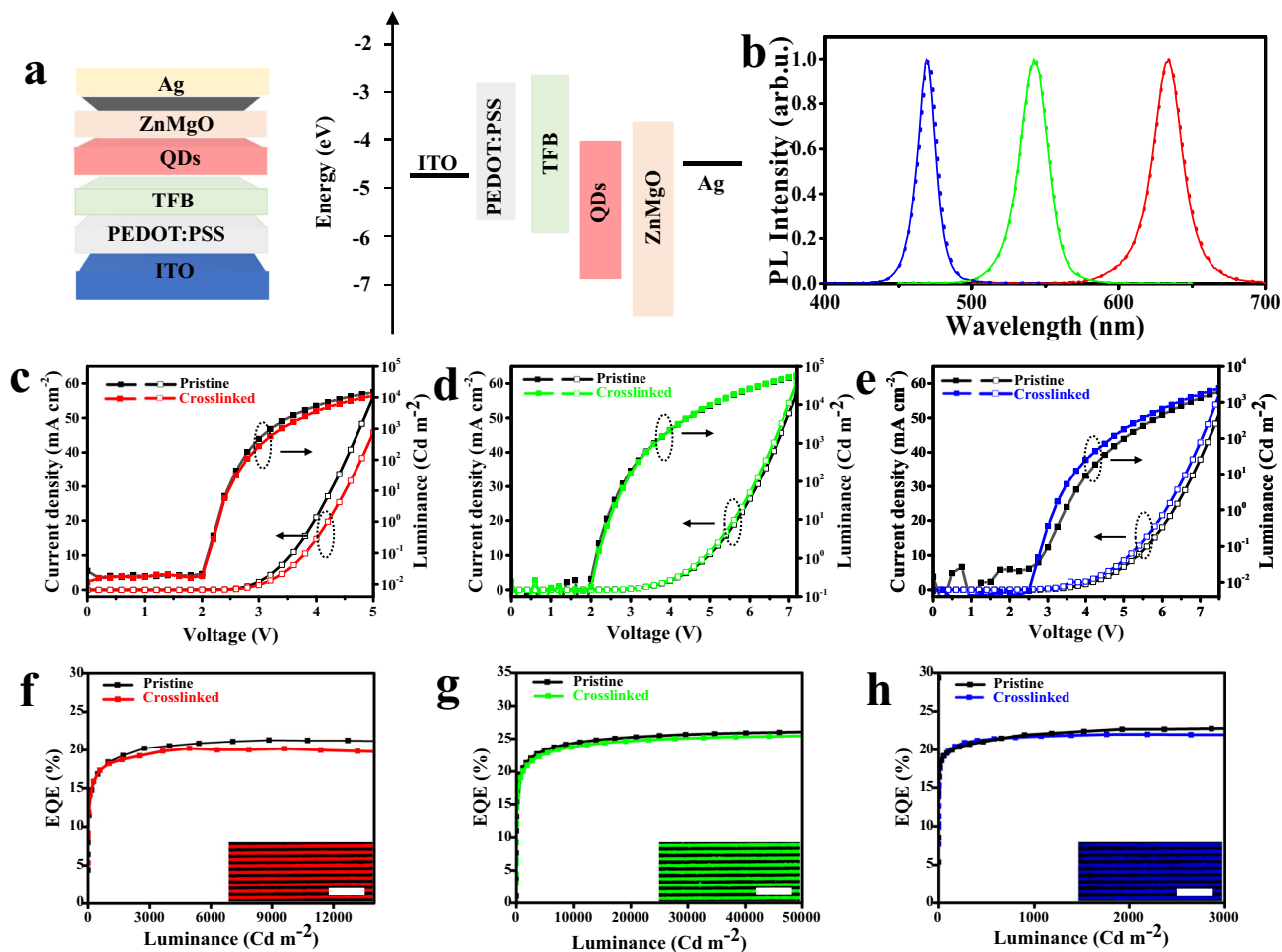


Fig. 7 | Cd-based QLEDs performance. **a** Schematic device structure and energy band diagram of a representative QLEDs. **b** Comparison of the EL spectra of pristine (dashed) and crosslinked (solid) QLEDs. **c–e** Current density–voltage–luminance of

pristine and crosslinked red-, green-, and blue-emitting QLEDs. **f–h** EQEs characteristics of pristine and crosslinked red, green, and blue QLEDs. Inset: EL images of pixelated red, green, and blue QLEDs. Scale bars, 10 μm.

patterning process. In Supplementary Fig. 39, the high efficiency of both pristine and crosslinked QLEDs devices are maintained in a wide range of brightness. The peak current efficiency (CE) of crosslinked red-, green- and blue-emitting QLEDs is 25.1, 94.7, and 12.5 cd A⁻¹, respectively, which is also close to that of pristine QLEDs. These positive effects are mainly attributed to higher carrier concentration and hole mobility in QDs layers with added TPP molecules⁵⁸. As shown in Supplementary Fig. 40, introducing TPP results in an upward shift of the valence band maximum (VBM) for red-, green-, and blue-emitting QDs. For instance, the VBM of blue QDs increases from -7.02 eV (pristine) to -6.72 eV (with TPP), and further to -6.56 eV after photochemical cross-linking. This upward shift causes an effective reduction of the energy barrier for hole injection from the neighboring HTL into the QDs, thereby promoting improved charge balance within the emissive layer. However, the increase in hole transport rate compensates for the reduction in electron mobility, resulting in no significant net improvement in crosslinked device performance.

We further test the performance of QLEDs devices with crosslinked Cd-free QDs (red-emitting InP/ZnS, green and blue-emitting, ZnSe/ZnS) active layers (Supplementary Fig. 41). Compared to pristine devices, the crosslinked QLEDs exhibit nearly identical *J-V-L* characteristics, and there is no noticeable change in the EL peak wavelength or spectral width (Supplementary Fig. 42). These results validate that the TPP-mediated patterning method is compatible with Cd-free-based QDs, and enables functional device fabrication without the need for Cd-based emitters. While the performance does not yet

match that of Cd-based devices, we emphasize that this discrepancy primarily reflects the current state-of-the-art in QDs material development, rather than limitations of the patterning method itself. Therefore, the observed device characteristics strongly suggest that the direct optical patterning process using TPP has the potential to realize practical EL displays.

Benefiting from the excellent patterning fidelity and stable QLEDs performance, we further demonstrate the direct photolithographic patterning of QDs on TFT backplanes, achieving successful integration of QLEDs with TFT circuitry to fabricate an active-matrix QLED (AM-QLED) display. In contrast to previous demonstrations, where only red and green AM-QLEDs could be achieved via photolithographic patterning⁵⁹, we report the successful integration of blue QDs into TFT circuits. This enables us to realize a full-color AM-QLEDs display by integrating RGB QDs onto the TFT backplane using our TPP-based DOLFIN technique.

The TFT backplane used in our demonstration consists of a pixel array designed specifically for the fabrication of AM-QLEDs displays. As illustrated in Fig. 8a, each pixel unit consist of three TFTs. TFT-1 is activated by a scan voltage (V_{scan}) and data voltage (V_{data}), which in turn triggered TFT-2 through a direct connection between the drain of TFT-1 and the gate of TFT-2. Upon activation, a power supply signal (V_{dd}) is applied to the source of TFT-2 and delivered to the drain to drive the QLEDs pixel. TFT-3 is used to reset the potential of TFT-2 in preparation for the next input signal cycle. Our strategy enables QDs patterning on two types of TFT backplanes with different pixel sizes,

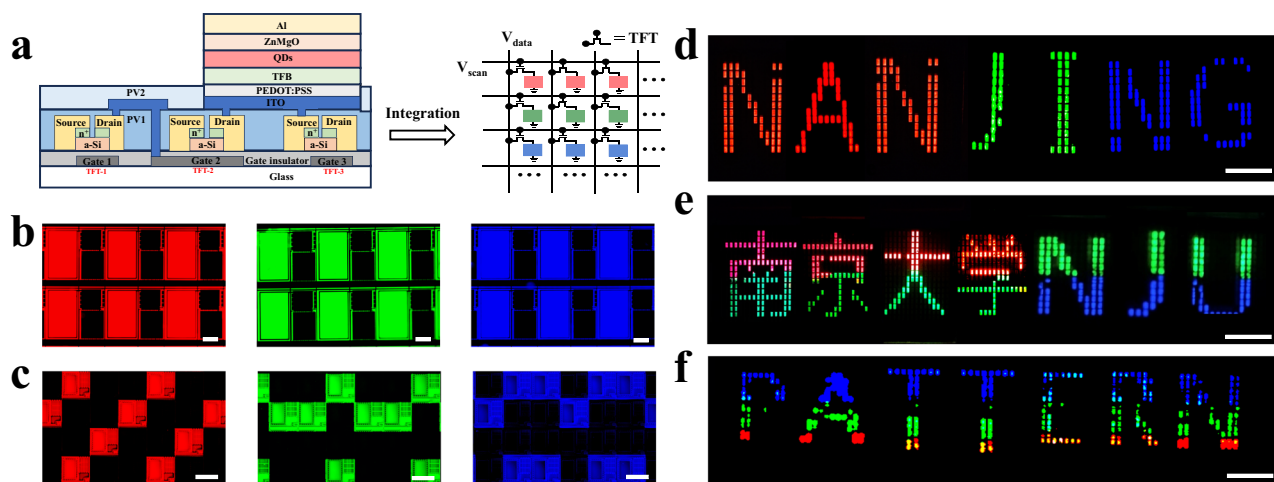


Fig. 8 | Active-matrix QLEDs displays. **a** Schematic and structure of the pixel drive circuit consisting of three TFTs (address TFT-1, drive TFT-2, and reset TFT-3) and a storage capacitor. The layers (PEDOT: PSS, TFB, QDs, ZnO) were spin-coated on the TFT backplane with a grounded co-cathode. TFT-1, controlled by scan voltage (V_{scan}) and data voltage (V_{data}), biases TFT-2 to drive the QLED, while TFT-3 resets the potential for the next operation. PV1 and PV2 are passivation layers. a-Si and n⁺ denote amorphous silicon and n-type doping. **b** Patterned QLEDs displays

fabricated on large-size TFT backplanes with RGB sub-pixels of $380 \times 650 \mu\text{m}$ and a resolution of 19 ppi. Scale bars, $200 \mu\text{m}$. **c** Patterned QLEDs displays fabricated on small-size TFT backplanes. Right: integration of single-color QDs on TFT backplanes with RGB sub-pixel dimensions of $85 \times 140 \mu\text{m}$ and a resolution of 77 ppi. Scale bars, $200 \mu\text{m}$. EL images of QLED displays with single- (**d**), dual- (**e**), and ternary- (**f**) color patterns of red, green, and blue QD layers, showing the images of letters, numbers, symbols, and Chinese characters. Scale bars, 1 cm.

where each patterned monochromatic QLEDs functions as a subpixel. We pattern QD layers into a 16×16 pixel array (Fig. 8b), precisely aligned in both size and position with the underlying TFT architecture (Supplementary Fig. 43), thereby enabling deterministic control of charge injection into each QLED pixel. On the large-area TFT backplane, the RGB subpixel dimensions are $380 \times 650 \mu\text{m}$. Additionally, we fabricate patterned QLEDs displays on a smaller pixel TFT backplane, where the RGB subpixel size is reduced to $85 \times 140 \mu\text{m}$, achieving a resolution of 77 pixels per inch (ppi) (Fig. 8c and Supplementary Fig. 44), the highest resolution reported to date for full-color AM-QLEDs fabricated using the DOLFIN approach. It is worth noting that this resolution is limited by the minimum achievable TFT pixel size, rather than by the resolution of the TPP-based patterning process itself. This underscores the tremendous potential of our method for future industrial-scale fabrication of high-resolution, full-color micro-displays using DOLFIN.

Finally, we demonstrate pixel-level active-matrix control for the display of letters, numbers, and even Chinese characters transmitted via Bluetooth from a computer (Fig. 8d–f and Supplementary Videos 1–4). In single-color display mode, uniform emission from individual pixels results in vivid and well-defined images. In dual-color and full-color display modes, complex Chinese characters such as “Nanjing University” and the text “NJU” and “DOLFIN” are rendered in multiple colors. With further optimization of QD structure, surface chemistry, and device architecture, we anticipate continued enhancement in the performance of full-color QDs-based displays.

Discussion

In summary, we develop a multifunctional patterning strategy based on a commercially available small molecule TPP, that enables ambient-condition, photoresist-free lithography of QDs with high-resolution and preserved optoelectronic properties. Acting simultaneously as a surface ligand, photosensitizer, and oxidation protector, TPP triggers oxygen-mediated photochemical reactions under UV exposure, facilitating precise modulation of QDs solubility without degradation. This strategy achieves full-color QDs patterning with a resolution up to 9534 dpi and facilitated the fabrication of electroluminescent QLEDs with EQEs—21.6% for blue, 25.6% for green, and 20.2% for red—matching or exceeding the unpatterned counterparts. The integration

of patterned RGB QDs with TFT backplanes further enables the demonstration of a full-color active-matrix QLEDs display based entirely on ambient-condition photolithography. Therefore, the TPP-enabled patterning strategy offers versatile guidance for future design of multifunctional small molecules tailored to specific QDs systems and device architectures. By rationally tuning molecular structures and functional groups, it may be possible to optimize radical generation efficiency, photoreactivity, and compatibility with various QDs surface chemistries—including emerging heavy-metal-free (e.g., InP- and ZnSe-based) QDs. Furthermore, exploring broader photonic excitation sources beyond UV, such as near-UV or visible light, could enable milder, substrate-friendly processes and further expand application scenarios. Together, these advances would accelerate the commercial translation of high-resolution, photoresist-free QDs patterning for next-generation full-color displays and flexible optoelectronic devices, supporting the industry’s shift toward Cd-free, environmentally sustainable solutions.

Methods

Materials

The following chemicals and materials are used as received. Cadmium oxide (CdO, 99.99%, Aladdin), selenium powder (Se, 200 mesh, 99.999% metals basis, Aladdin), TOP (97%, Strem), trioctylphosphine oxide (TOPO, 90%, Aladdin), TPP (99%, Aladdin), OA (90%, Alfa Aesar), oleylamine (OLAm, 95%, Strem), octadecene (ODE, 90%, Alfa Aesar), cesium carbonate (Cs_2CO_3 , 99.9% trace metals basis, Aldrich), lead (II) bromide (PbBr_2 , 99.999% metals basis, Alfa Aesar), methyl acetate (MeOAc, anhydrous, 99.5%, Aldrich), tetrachloroauric(III) acid trihydrate ($\text{HAuCl}_4 \cdot 3\text{H}_2\text{O}$, 99%, Innochem), 1,2,3,4-tetrahydronaphthalene, (tetralin, 97%, Alfa Aesar), tetrabutylammonium bromide (TBAB, 99%, Aladdin), Nickel(II) acetylacetonate ($\text{Ni}(\text{acac})_2$, 95%, Sigma-Aldrich), Benzyl ether (BE, 98%, Sigma-Aldrich), isopropanol (Aladdin), zinc acetate dihydrate (Aladdin), 1-dodecanethiol (Aladdin), hexane (anhydrous, 95%, Aldrich), ethanol (anhydrous, 99.5%, Aldrich), and dimethylformamide (DMF, >99.7%, Alfa Aesar). Poly(3,4-ethylenedioxythiophene)-poly(styrenesulfonate) (PEDOT:PSS, Clevious™ PVP, Al 4083, 1.3–1.7% aqueous solution) and poly[(9,9-dioctylfluorenyl-2,7-diyl)-co-(4,4'-(N-(4-sec-butylphenyl)diphenylamine))] (TFB, average molecular weight, $\sim 50,000 \text{ g mol}^{-1}$, American Dye Source) are used as

hole injection and transport materials, respectively. ZnMgO QDs (30 mg mL⁻¹ in ethanol, Mesolight) serve as the ETL. II–VI semiconductor QDs with core/shell or core/shell/shell structures and red (CdSe/ZnS), green (CdSe/CdZnSeS/ZnS), and blue (CdZnS/ZnS) are obtained from TCL Inc. Heavy-metal-free InP/ZnS (capped with OA and OLA ligands) are purchased from Suzhou Xingshuo Nanotech Co. Ltd (Mesolight).

Synthesis of wurtzite CdSe quantum dots

Wurtzite CdSe QDs capped with OA are synthesized using cadmium oleate as the Cd precursor, following a modified literature procedure⁶⁰. Cd(OA)₂ (2.25 mL), TOPO (1.2 × g), and ODE (12 mL) are loaded into a 100 mL three-necked flask, dried under vacuum at 70 °C for 1 h, and heated to 300 °C under nitrogen. A stock solution containing TOP-Se (4 mL, 1 mol L⁻¹) in TOP and OLAm (3 mL) is swiftly injected at 300 °C. The reaction is maintained at 280 °C for 2–3 min, then cooled to room temperature. The QDs are isolated by ethanol precipitation, centrifugation, and redispersion in hexane. To prepare Cd(OA)₂ stock solution, CdO (0.643 × g, 5 mmol) is mixed with OA (10 mL) in a 25 mL three-neck flask at room temperature and heated under vacuum at 100 °C for 1 h. The mixture is then heated to 250 °C under nitrogen until a colorless solution formed, indicating completion of Cd(OA)₂ formation. After cooling, the solution is dried under vacuum at 150 °C to remove residual water, yielding Cd(OA)₂ as a white solid for further use.

Synthesis of Au nanocrystals

Au nanocrystals (NCs) are prepared following a previously reported procedure⁶¹. HAuCl₄·3H₂O (0.1 × g, 0.25 mmol) is dissolved in a mixture of tetralin (10 mL) and OLAm (10 mL) in a 50 mL flask at room temperature. The solution is purged with nitrogen and stirred for 15 min, during which a light red color developed. Separately, TBAB (0.0435 × g, 0.13 mmol) is dissolved in tetralin (1 mL) and OLAm (1 mL) and rapidly injected into the flask. The reaction proceeds under nitrogen for 1 h. The resulting Au NCs are purified by six cycles of hexane/ethanol washing, dispersed in toluene at 40 mg mL⁻¹, and stored at 4 °C for further use.

Synthesis of Ni nanocrystals

Monodisperse Ni NCs capped with OLAm are synthesized via thermal decomposition of Ni(acac)₂⁶². For the preparation of 12.5 nm Ni NCs, Ni(acac)₂ (300 mg) and OLAm (4 mL) are dissolved in benzyl ether (30 mL). The mixture is evacuated at room temperature for 15 min, flushed with nitrogen, and then TOP (1.304 mL) is added. After a second evacuation, the solution is heated to 100 °C and subsequently reacted at 230 °C under magnetic stirring for 15 min. The NCs are isolated by addition of isopropanol followed by centrifugation (8000 rpm, 3 min) and redispersed in hexanes for further use.

Synthesis of ZnO nanocrystals

ZnO NCs are synthesized according to a previously reported method⁶³. Zn(OA)₂·2H₂O (1 g, 45 mmol) is dissolved in isopropanol (250 mL) and heated to 60 °C in an oil bath. Separately, NaOH (0.29 × g, 73 mmol) is dissolved in isopropanol (85 mL) at room temperature and then added to the zinc precursor solution, with the reaction maintained at 60 °C. After 30 min, 1-dodecanethiol (1.09 mL) is introduced dropwise, leading to the gradual appearance of turbidity. The reaction is continued for 60 min with heating and stirring, after which the dispersion was allowed to settle. The supernatant is removed, and the nanocrystals are collected by transferring the mixture into centrifuge tubes, followed by ethanol washing and precipitation via centrifugation (3500 rpm, 2 min).

Characterizations

Scanning electron microscopy (SEM) is carried out using a Zeiss Supra 55 field-emission microscope. TEM is performed on a JEOL JEM-2800

instrument operated at 120 kV. X-ray diffraction patterns are collected on a Bruker D8 ADVANCE diffractometer equipped with Cu K α radiation. Fourier transform infrared (FT-IR) spectra are recorded on a Tensor II spectrometer (Bruker). Film roughness and thickness are determined using a Bruker Icon atomic force microscope (AFM) and a Dektak-XT profilometer. Bright-field and fluorescence images are acquired with a Nikon Ni-U fluorescence microscope. UV–vis absorption spectra are obtained on an Agilent Cary 5000 spectrophotometer. Steady-state fluorescence spectra and absolute PLQYs are measured using a Lab-sphere integrating sphere coupled to a computer-controlled spectrometer. Time-resolved photoluminescence is recorded on a HORIBA FL-3 3D fluorescence spectrometer. NMR spectra are measured on a Bruker AVANCE III-500 instrument. EPR measurements are conducted on a Bruker EMX Plus spectrometer under in situ UV irradiation.

Patterning procedures

Photoresist-free photopatterning is carried out in three steps. (i) Film coating. Quartz, silicon, or glass substrates are sequentially sonicated in toluene, acetone, methanol, and ethanol (15 min each) and dried under nitrogen. Purified QDs (20–30 mg mL⁻¹ in toluene or octane) are blended with TPP (10–40 wt%) and spin-coated at 2000 rpm for 40 s. (ii) UV exposure. The films are contacted with photomasks and irradiated using a handheld UV lamp (254 nm, 4.5 mW cm⁻²). (iii) Development. Unexposed QDs are removed by dynamically spin-coating the same solvent (2000 rpm, 30 s). All procedures are conducted in a cleanroom under yellow light. Typical patterning involves 10–40 wt% TPP and UV doses of 40–270 mJ cm⁻², depending on QD type and ligand coverage.

Quantum dots devices fabrication

Pristine and patterned QLEDs (non-arrayed) are fabricated in a conventional device architecture consisting of indium tin oxide (ITO)/PEDOT:PSS/TFB/QDs/ZnMgO/Ag. ITO substrates are sequentially sonicated in detergent, deionized water, acetone, and isopropanol (15 min each) and treated with oxygen plasma for 20 min. PEDOT:PSS is deposited by spin-coating at 5000 rpm and baked at 140 °C for 15 min. The samples are then transferred into a nitrogen glovebox for deposition of the TFB layer (25 nm), spin-coated at 3000 rpm for 30 s and annealed at 200 °C for 30 min. For pristine devices, QDs in octane (10–20 mg mL⁻¹) are spin-cast at 2000 rpm for 30 s and annealed at 80 °C for 10 min. For patterned devices, QDs premixed with 10–40 wt% TPP are spin-coated, irradiated with 254 nm UV light (40–270 mJ cm⁻²), and developed in octane; unless otherwise specified, the full film is exposed for direct comparison of performance. The ZnMgO ETL (35 nm) is deposited by spin-coating at 2000 rpm for 30 s, followed by annealing at 80 °C for 30 min. A 100 nm Ag cathode is then thermally evaporated under high vacuum (10⁻⁶ mbar). Devices are encapsulated with UV-curable epoxy and glass covers prior to electrical and optical characterization. Current density–voltage–luminance (J–V–L) characteristics and angular emission profiles are measured using a Keithley 2614B source meter and a calibrated PIN-25D silicon photodiode.

For proof-of-concept active-matrix QLED displays, patterned emissive layers are integrated onto 16 × 16 TFT backplanes. On top of the patterned ITO electrodes, sequential layers of PEDOT:PSS, TFB, photopatterned QDs, ZnMgO, and an Al cathode are deposited using procedures analogous to those above. The QD layer is patterned through a designed photomask to align with the underlying ITO array. Mono-, dual-, and full-color displays are fabricated using red-, green-, and blue-emitting QDs. The completed devices are connected to custom display drivers via hot-pressed wiring and operated under computer control via Bluetooth.

Reporting summary

Further information on research design is available in the Nature Portfolio Reporting Summary linked to this article.

Data availability

The main data that support the findings of this study are available in this article and its Supplementary Information. Additional data are available from the corresponding author upon request.

References

1. Kagan, C. R., Lifshitz, E., Sargent, E. H. & Talapin, D. V. Building devices from colloidal quantum dots. *Science* **353**, aac5523 (2016).
2. Wang, W. et al. Colloidal inorganic ligand-capped nanocrystals: fundamentals, status, and insights into advanced functional nano-devices. *Chem. Rev.* **122**, 4091–4162 (2021).
3. Shu, Y. et al. Quantum dots for display applications. *Angew. Chem. Int. Ed.* **59**, 22312–22323 (2020).
4. Li, X. et al. Bright colloidal quantum dot light-emitting diodes enabled by efficient chlorination. *Nat. Photonics* **12**, 159–164 (2018).
5. Bian, Y. et al. Efficient green InP-based QD-LED by controlling electron injection and leakage. *Nature* **635**, 854–859 (2024).
6. Kim, D. C. et al. Intrinsically stretchable quantum dot light-emitting diodes. *Nat. Electron.* **7**, 365–374 (2024).
7. Song, J. et al. Over 30% external quantum efficiency light-emitting diodes by engineering quantum dot-assisted energy level match for hole transport layer. *Adv. Funct. Mater.* **29**, 1808377 (2019).
8. Deng, Y. et al. Solution-processed green and blue quantum-dot light-emitting diodes with eliminated charge leakage. *Nat. Photonics* **16**, 505–511 (2022).
9. Chen, X. et al. Blue light-emitting diodes based on colloidal quantum dots with reduced surface-bulk coupling. *Nat. Commun.* **14**, 284–392 (2023).
10. Kim, J., Roh, J., Park, M. & Lee, C. Recent advances and challenges of colloidal quantum dot light-emitting diodes for display applications. *Adv. Mater.* **36**, 2212220 (2024).
11. Park, S. Y., Lee, S., Yang, J. & Kang, M. S. Patterning quantum dots via photolithography: a review. *Adv. Mater.* **35**, 2300546 (2023).
12. Yoo, J. et al. Highly efficient printed quantum dot light-emitting diodes through ultrahigh-definition double-layer transfer printing. *Nat. Photonics* **18**, 1105–1112 (2024).
13. Kim, G. Y. et al. Chiral 3D structures through multi-dimensional transfer printing of multilayer quantum dot patterns. *Nat. Commun.* **15**, 6996–7006 (2024).
14. Xiang, C. et al. High efficiency and stability of ink-jet printed quantum dot light emitting diodes. *Nat. Commun.* **11**, 1646–1654 (2020).
15. Wei, C. et al. A universal ternary-solvent-ink strategy toward efficient inkjet-printed perovskite quantum dot light-emitting diodes. *Adv. Mater.* **34**, e2107798 (2022).
16. Wang, Y., Fedin, I., Zhang, H. & Talapin, D. V. Direct optical lithography of functional inorganic nanomaterials. *Science* **357**, 385–388 (2017).
17. Wang, Y., Pan, J. A., Wu, H. & Talapin, D. V. Direct wavelength-selective optical and electron-beam lithography of functional inorganic nanomaterials. *ACS Nano* **13**, 13917–13931 (2019).
18. Hahm, D. et al. Surface engineered colloidal quantum dots for complete green process. *ACS Appl. Mater. Interfaces* **12**, 10563–10570 (2020).
19. Ko, J., Ma, K., Joung, J. F., Park, S. & Bang, J. Ligand-assisted direct photolithography of perovskite nanocrystals encapsulated with multifunctional polymer ligands for stable, full-colored, high-resolution displays. *Nano Lett.* **21**, 2288–2295 (2021).
20. Fu, Z. et al. Direct photo-patterning of efficient and stable quantum dot light-emitting diodes via light-triggered, carbocation-enabled ligand stripping. *Nano Lett.* **23**, 2000–2008 (2023).
21. Hu, Z., Shu, Y., Qin, H., Hu, X. & Peng, X. Water effects on colloidal semiconductor nanocrystals: correlation of photophysics and photochemistry. *J. Am. Chem. Soc.* **143**, 18721–18732 (2021).
22. Zhang, J., Li, J., Ye, Z., Cui, J. & Peng, X. Hot-electron-induced photochemical properties of CdSe/ZnSe core/shell quantum dots under an ambient environment. *J. Am. Chem. Soc.* **145**, 13938–13949 (2023).
23. Noh, S. H. et al. Photocrosslinkable zwitterionic ligands for perovskite nanocrystals: self-assembly and high-resolution direct patterning. *Adv. Funct. Mater.* **33**, 2304004 (2023).
24. Hahm, D. et al. Direct patterning of colloidal quantum dots with adaptable dual-ligand surface. *Nat. Nanotechnol.* **17**, 952–958 (2022).
25. Lu, S. et al. Beyond a linker: the role of photochemistry of cross-linkers in the direct optical patterning of colloidal nanocrystals. *Angew. Chem. Int. Ed.* **61**, e202202633 (2022).
26. Nie, Q. et al. Direct optical patterning of quantum dot light-emitting diodes based on ultrafast, low-energy, site-controlled click chemistry reaction. *Adv. Funct. Mater.* **35**, 2420829 (2025).
27. Zhai, Z. et al. Nondestructive direct photolithography of colloidal quantum dots enabled by benzophenone-based crosslinkers. *Nano Res.* **18**, 94907980 (2025).
28. Wu, Q. et al. Homogeneous ZnSeTeS quantum dots for efficient and stable pure-blue LEDs. *Nature* **639**, 633–638 (2025).
29. Li, H. et al. Nanosurface-reconstructed perovskite for highly efficient and stable active-matrix light-emitting diode display. *Nat. Nanotechnol.* **19**, 638–645 (2024).
30. Morad, V. et al. Designer phospholipid capping ligands for soft metal halide nanocrystals. *Nature* **626**, 542–548 (2023).
31. Panzer, R. et al. Versatile Tri(pyrazolyl)phosphanes as phosphorus precursors for the synthesis of highly emitting InP/ZnS quantum dots. *Angew. Chem. Int. Ed.* **56**, 14737–14742 (2017).
32. Min, H., Ji, S.-G. & Seok, S. I. Relaxation of externally strained halide perovskite thin layers with neutral ligands. *Joule* **6**, 2175–2185 (2022).
33. Wu, J. et al. Efficient and stable thin-film luminescent solar concentrators enabled by near-infrared emission perovskite nanocrystals. *Angew. Chem. Int. Ed.* **59**, 7738–7742 (2020).
34. Zhang, X. et al. Conductive colloidal perovskite quantum dot inks towards fast printing of solar cells. *Nat. Energy* **9**, 1378–1387 (2024).
35. Liu, Z. et al. Efficient intramolecular charge-transfer fluorophores based on substituted triphenylphosphine donors. *Angew. Chem. Int. Ed.* **60**, 15049–15053 (2021).
36. Xiong, W. & Hu, D. Y. Fabrication of phosphonium bamboo cellulose by triphenylphosphine: preparation, characterization, and adsorption of Acid Black 24. *Environ. Sci. Pollut. R.* **26**, 1880–1891 (2019).
37. Heuer-Jungemann, A. et al. The role of ligands in the chemical synthesis and applications of inorganic nanoparticles. *Chem. Rev.* **119**, 4819–4880 (2019).
38. Anderson, N. C., Chen, P. E., Buckley, A. K., De Roo, J. & Owen, J. S. Stereoelectronic effects on the binding of neutral Lewis bases to CdSe nanocrystals. *J. Am. Chem. Soc.* **140**, 7199–7205 (2018).
39. Xiao, P. et al. Surface passivation of intensely luminescent all-inorganic nanocrystals and their direct optical patterning. *Nat. Commun.* **14**, 49 (2023).
40. Liu, D. et al. Direct optical patterning of perovskite nanocrystals with ligand cross-linkers. *Sci. Adv.* **8**, eabm8433 (2022).
41. Maeng, S. et al. Direct photocatalytic patterning of colloidal emissive nanomaterials. *Sci. Adv.* **9**, eadi6950 (2023).
42. Liu, Q. et al. Visible-light-induced selective photolysis of phosphonium iodide salts for monofluoromethylations. *Angew. Chem. Int. Ed.* **60**, 25477–25484 (2021).
43. Lv, C., He, C. & Pan, X. Oxygen-initiated and regulated controlled radical polymerization under ambient conditions. *Angew. Chem. Int. Ed.* **57**, 9430–9433 (2018).
44. Zhang, J. et al. Enhanced polyacrylamide degradation via OH radical-initiated single-electron transfer. *ACS Omega* **8**, 46589–46597 (2023).

45. Simon, T. et al. Redox shuttle mechanism enhances photocatalytic H₂ generation on Ni-decorated CdS nanorods. *Nat. Mater.* **13**, 1013–1018 (2014).
46. Xu, H. et al. Toward advanced sodium-ion batteries: a wheel-inspired yolk-shell design for large-volume-change anode materials. *J. Mater. Chem. A* **6**, 13153–13163 (2018).
47. Emara, M. M. & Van Patten, P. G. Effect of oxygen and polymer matrix on photo-induced changes in CdSe quantum dots. *Mater. Chem. Phys.* **256**, 123652–123660 (2020).
48. Kusterer, R., Ruhmlieb, C., Strelow, C., Kipp, T. & Mews, A. Reversible and irreversible effects of oxygen on the optical properties of CdSe quantum wires. *J. Phys. Chem. C* **126**, 19240–19249 (2022).
49. Hines, D. A., Becker, M. A. & Kamat, P. V. Photoinduced surface oxidation and its effect on the exciton dynamics of CdSe quantum dots. *J. Phys. Chem. C* **116**, 13452–13457 (2012).
50. Kim, M. J. et al. Universal three-dimensional crosslinker for all-photopatterned electronics. *Nat. Commun.* **11**, 1 (2020).
51. Batesky, D. C., Goldfogel, M. J. & Weix, D. J. Removal of triphenylphosphine oxide by precipitation with zinc chloride in polar solvents. *J. Org. Chem.* **82**, 9931–9936 (2017).
52. Wang, N., Ma, T., Yu, X., Xu, L. & Zhang, R. Determination of peroxide values of edible oils by ultraviolet spectrometric method. *Food Anal. Method.* **9**, 1412–1417 (2015).
53. Schraml, J., Čapka, M. & Blechta, V. ³¹P and ¹³C NMR spectra of cyclohexylphenylphosphines, tricyclohexylphosphine and triphenylphosphine. *Magn. Reson. Chem.* **30**, 544–547 (2005).
54. Zeldin, M., Mehta, P. & Vernon, W. D. Phosphorus-31 N. M. R. of triphenylphosphine oxide complexes with compounds of silicon, germanium, and tin. *Inorg. Chem.* **18**, 463–466 (1979).
55. Jo, J.-H. et al. Photostability enhancement of InP/ZnS quantum dots enabled by In₂O₃ overcoating. *J. Alloy. Compd.* **647**, 6–13 (2015).
56. Chen, Z. et al. Electrochemical replication and transfer for low-cost, sub-100 nm patterning of materials on flexible substrates. *Adv. Mater.* **35**, 2210778 (2023).
57. Yang, J. et al. Toward full-color electroluminescent quantum dot displays. *Nano Lett.* **21**, 26–33 (2021).
58. Min, C. et al. A Simple and effective phosphine-doping technique for solution-processed nanocrystal solar cells. *Nanomaterials* **13**, 1766–1776 (2023).
59. Fu, Z. et al. Direct photopatterning of colloidal quantum dots with electronically optimized diazirine cross-linkers. *J. Am. Chem. Soc.* **146**, 28895–28905 (2024).
60. Zhang, H., Jang, J., Liu, W. Y. & Talapin, D. V. Colloidal nanocrystals with inorganic halide, pseudohalide, and halometallate ligands. *ACS Nano* **8**, 7359–7369 (2014).
61. Peng, S. et al. A facile synthesis of monodisperse Au nanoparticles and their catalysis of CO oxidation. *Nano Res.* **1**, 229–234 (2008).
62. Cargnello, M. et al. Control of metal nanocrystal size reveals metal-support interface role for ceria catalysts. *Science* **341**, 771–773 (2013).
63. Sun, Y., Donaldson, P. D., Garcia-Barriocanal, J. & Swisher, S. L. Understanding quantum confinement and ligand removal in solution-based ZnO thin films from highly stable nanocrystal ink. *J. Mater. Chem. C* **6**, 9181–9191 (2018).
- China (22171132 and 52472165), the Program for Innovative Talents and Entrepreneurs in Jiangsu (020513006012 and 020513006014), and the Zijin Scholars Foundation (0205181022). D.V.T. acknowledges support from the National Science Foundation under Award No. CHE-2404291 and from the Department of Defense Air Force Office of Scientific Research under grant number FA9550-22-1-0283. Work performed at the Center for Nanoscale Materials, a U.S. Department of Energy Office of Science User Facility, was supported by the U.S. DOE, Office of Basic Energy Sciences, under Contract No. DE-AC02-06CH11357.

Author contributions

Y.W. conceived the concept of this work. J.M. and Y.Z. performed the lithography experimental work. J.G. and Y.Z. performed optical measurements. H.Z., L.Z., and W.H. performed the device measurements. P.Z. provided suggestions on the AFM experiments. J.G., L.Y., and X.D. integrated patterned RGB QDs with thin-film transistor (TFT) backplanes. Y.W., D.T., and J.G. designed the experiments, analyzed the data, and co-wrote the paper. H.Z. and X.D. assisted Y.W. in polishing the manuscript. Y.W. and D.T. supervised the project. All authors discussed the results and commented on the manuscript.

Competing interests

The authors declare no competing interests.

Additional information

Supplementary information The online version contains supplementary material available at <https://doi.org/10.1038/s41467-025-64696-1>.

Correspondence and requests for materials should be addressed to Dmitri V. Talapin or Yuanyuan Wang.

Peer review information *Nature Communications* thanks Yuchen Wu, Ting Zhang, who co-reviewed with Chang Gu, and the other anonymous reviewer(s) for their contribution to the peer review of this work. A peer review file is available.

Reprints and permissions information is available at <http://www.nature.com/reprints>

Publisher's note Springer Nature remains neutral with regard to jurisdictional claims in published maps and institutional affiliations.

Open Access This article is licensed under a Creative Commons Attribution-NonCommercial-NoDerivatives 4.0 International License, which permits any non-commercial use, sharing, distribution and reproduction in any medium or format, as long as you give appropriate credit to the original author(s) and the source, provide a link to the Creative Commons licence, and indicate if you modified the licensed material. You do not have permission under this licence to share adapted material derived from this article or parts of it. The images or other third party material in this article are included in the article's Creative Commons licence, unless indicated otherwise in a credit line to the material. If material is not included in the article's Creative Commons licence and your intended use is not permitted by statutory regulation or exceeds the permitted use, you will need to obtain permission directly from the copyright holder. To view a copy of this licence, visit <http://creativecommons.org/licenses/by-nc-nd/4.0/>.

© The Author(s) 2025

Acknowledgements

This work was supported by the National Key R&D Program of China (2022YFB3607000), the Science and Technology Program in Jiangsu Province (BK20232041), the National Natural Science Foundation of